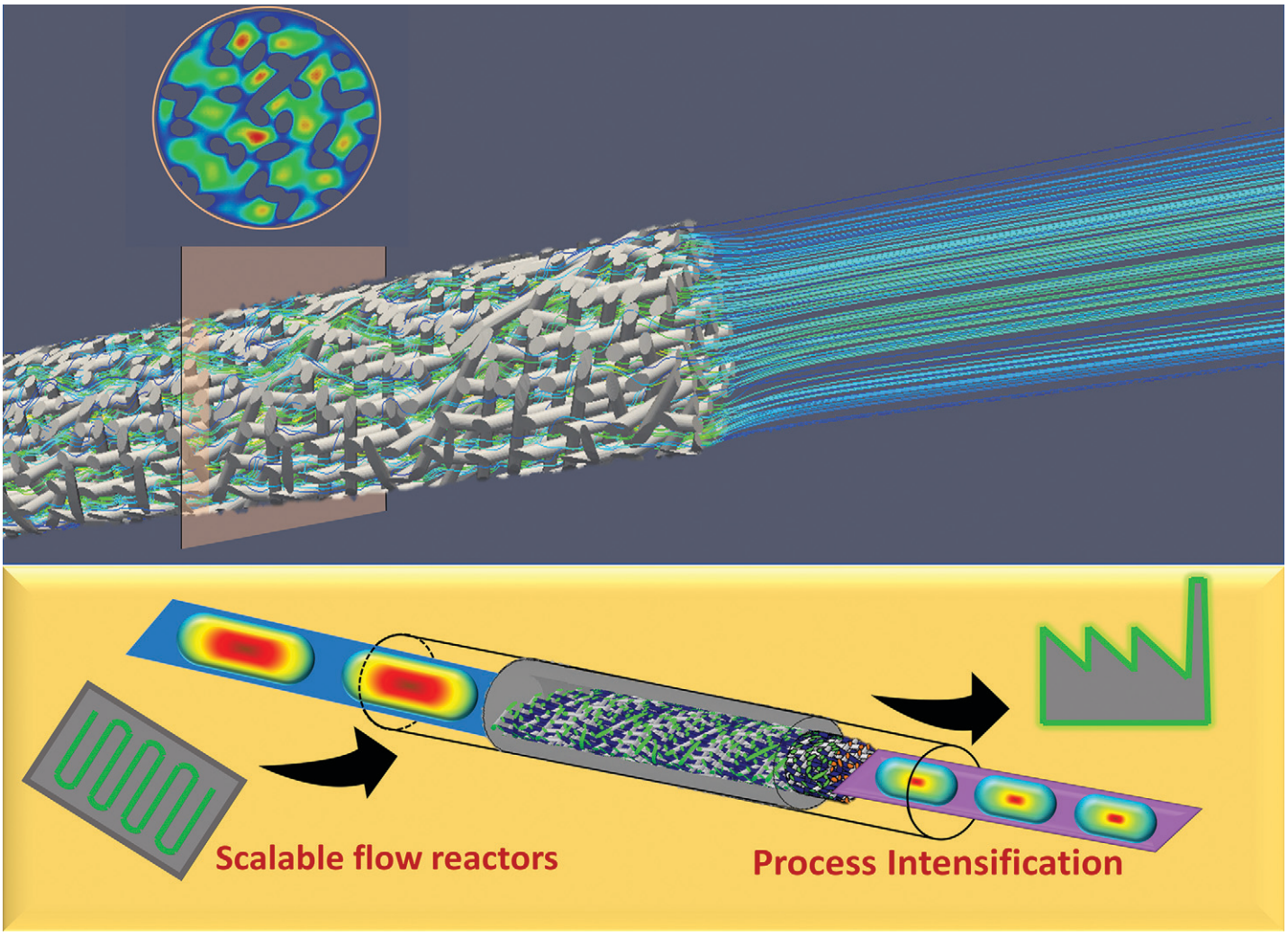

Highlighting research from the Transport Phenomena and Multiphase Systems Group at the Department of Chemical Engineering, KU Leuven.

Designed porous milli-scale reactors with enhanced interfacial mass transfer in two-phase flows

The influence of geometrical parameters of 3D printed designed porous reactors on hydrodynamics and interfacial transport is systematically studied for different two-phase flow regimes using optical and chemical measurements.

As featured in:

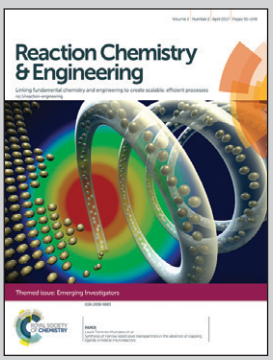

See Simon Kuhn *et al.*, *React. Chem. Eng.*, 2017, **2**, 137.

ROYAL SOCIETY OF CHEMISTRY

rsc.li/reaction-engineering

Registered charity number: 207890

Reaction Chemistry & Engineering

PAPER

View Article Online
View Journal | View Issue

Cite this: *React. Chem. Eng.*, 2017, **2**, 137

Designed porous milli-scale reactors with enhanced interfacial mass transfer in two-phase flows

Aditi Potdar,[a] Lidia N. Protasova,[b] Leen Thomassen[ac] and Simon Kuhn*[a]

Received 7th October 2016,
Accepted 5th December 2016

DOI: 10.1039/c6re00185h

rsc.li/reaction-engineering

The hydrodynamics and mass transfer characteristics in liquid–liquid flow through various structured and well-defined porous reactors are characterized using laser based optical measurements (PIV and PLIF) in combination with chemical extraction methods. We investigate both high and low interfacial tension fluid systems (toluene–water and *n*-butanol–water), and we have identified that depending on the fluid properties different design parameters of the porous structures play a crucial role in determining the overall mass transfer performance. In general, the porous reactors enhance slug breakup, resulting in lower mean slug lengths for both phases compared to an empty tube and an associated enhancement in surface renewal velocities. The designed porous milli-scale reactors provide enhanced mass transfer performance, with an order of magnitude reduced energy dissipation compared to conventional milli-scale packed bed reactors.

1. Introduction

Microreaction technology has evolved into an established tool for chemical synthesis[1,2] and reaction automation[3] on a laboratory scale. This is driven by the enhanced mass and heat transfer coefficients obtained by decreasing the characteristic reactor length scale and thus increasing the surface-to-volume ratio. Furthermore, microreaction technology allows for safer operation, which then enables synthesis at elevated temperatures and pressures,[4] which in turn allows access to novel process windows[5,6] to further intensify the involved chemical processes. Especially in the field of pharmaceuticals, these developments have led to the integration of microreactors into continuous-flow production.[7–10]

Most of the relevant chemical transformations involve multiple immiscible phases, and for fast reaction kinetics, interfacial mass transfer then becomes the rate limiting step. The interfacial mass transfer rate scales with the volumetric mass transfer coefficient k_La, and the comparison of experimentally obtained k_La values between conventional equipment and various microreactors for gas–liquid and liquid–liquid systems reveals larger mass transfer coefficients on the micro-scale.[11] In the case of solid catalyzed multiphase reactions, microstructured packed bed reactors are commonly used.[12,13] In these reactors, the solid catalyst particles are retained in the microchannel creating a porous structure, which increases both the interfacial mass transfer and the diffusion of the reactive species to the catalyst surface. In addition, it was also observed that for bi-phasic reactions using a phase transfer catalyst the presence of an inert packed bed will improve mixing leading to full conversion at lower residence times.[14] This is an important observation for scale-up, as increasing the fluid–structure interaction was shown to result in comparable volumetric mass transfer coefficients, k_La, across reactor length scales.[15] Consequently, packed beds represent a versatile reactor system to improve mixing and mass transfer for multiphase transformations. However, the main drawbacks limiting their use, especially for scale-up applications, is their large associated pressure drop, flow maldistribution resulting in non-uniform contact time, and attrition of small particles.

An interesting alternative to create porous structures similar to a packed bed is the use of open cell metal foams. Metal foam systems were initially developed for light weight construction,[16,17] but due to their superior thermal performance they were subsequently employed as compact heat exchangers.[18–21] Single phase hydrodynamic studies revealed that inserting metal foam structures into tubular reactors results in plug flow behaviour,[22,23] and the corresponding pressure drop is lower compared to the one observed in packed beds, primarily due the large void fraction of open cell foams.[22,24] A combined experimental and numerical approach identified the ligament shape and thickness of the foam structure as the key design parameters to enhance mixing *via* induced turbulent kinetic energy.[25–27] These

[a] *KU Leuven, Department of Chemical Engineering, Celestijnenlaan 200F, 3001 Leuven, Belgium. E-mail: simon.kuhn@kuleuven.be*
[b] *Flemish Institute for Technological Research – VITO, Boeretang 200, 2400 Mol, Belgium*
[c] *KU Leuven, Faculty of Industrial Engineering, Lab4U, Agoralaan Building B Box 8, 3590 Diepenbeek, Belgium*

hydrodynamic properties, combined with the large specific surface area of open cell foams, explain their use as internal mixers and as catalyst supports.[28] The design concept of these porous reactors is analogous to structured mixers, *e.g.* Sulzer type static mixers.[29,30] However, the use of open cell foams offers a more complex structure on the micro- and milli-scales, rendering them a flexible choice at these length scales.

In terms of multiphase flow, metal foams were primarily investigated for gas–liquid systems. An air–water system was used to study the hydrodynamics and mass transfer in both co-current and counter-current operations in solid foam packings of 5–40 pores per linear inch (ppi).[31–33] For counter-current operation, three flow regimes were identified, both bubble and pulsating flows for high liquid hold-up and trickle flow for low liquid hold-up. Furthermore, in the case of low liquid hold-up, the liquid side mass transfer coefficient increases with increasing ppi and liquid Reynolds number.[33] This behavior was not observed for the co-current operation, where the mass transfer coefficient is independent of the ppi but increases with increasing gas and liquid velocities.[32] In a recent study, a 2 mm square channel was filled with an open cell foam and developed gas–liquid Taylor flow was passed through it.[34,35] It was observed that the Taylor flow breaks up when it came into contact with the porous structure, inducing a pulsed flow with a considerable slip between the liquid and gas phases. The pulsing regime results in enhanced mixing and convective mass transport. Accordingly, when the same open cell foam was wash-coated with a Pd/Al_2O_3 catalyst and applied to hydrogenation, enhanced external mass transfer coefficients compared to those in fixed beds were observed.[36]

The above discussion highlights the potential of open cell foams as novel reactors for multiphase transformations, combining increased specific surface area with low pressure drops. However, the influence of the geometrical details (*e.g.* pore and ligament sizes, orientation) of the porous structure on two-phase hydrodynamics and interfacial mass transfer is not yet fully established. In this paper, we study liquid–liquid flow hydrodynamics and mass transfer in various structured and well-defined porous structures similar to open cell foams. We make use of rapid prototyping techniques (3D fibre deposition and selective laser sintering) which allow a systematic variation of the unit cell geometry. Using laser based optical measurements and chemical extraction methods, the impact of these geometric changes on two-phase flow hydrodynamics and interfacial mass transfer in two liquid–liquid systems (toluene–water and *n*-butanol–water) is investigated. We choose these two fluid systems to characterize different flow patterns, in which the two-phase flow of toluene–water is established as slug flow (or Taylor flow) in an empty tube, whereas that of *n*-butanol–water results in stratified flow (see Fig. 1 for a sketch of the two flow patterns). Furthermore, we benchmark the obtained results against those of an empty tube of the same inner diameter and packed beds of comparable void volume. The results of this study allow further design optimization of defined porous structures as novel reactors for continuous manufacturing.

Fig. 1 Two-phase flow patterns observed for the fluid systems toluene–water (left) and *n*-butanol–water (right) in an empty glass tube. Due to the differences in interfacial tension between the aqueous phase and the organic phase, the two-phase flow of toluene–water is established as slug flow (or Taylor flow), whereas that of *n*-butanol–water results in stratified flow.

2. Methods

2.1. Porous structures

We investigate various custom designed porous structures produced by either selective laser sintering (SLS,[37,38] manufactured by inspire AG, Switzerland) or 3-dimensional fibre deposition (3DFD,[39–41] manufactured by VITO, Belgium). The 3DFD samples were prepared using a modified CNC machine and extrusion system to build the structures layer by layer by computer controlled movements in the *x*, *y* and *z*-directions. All structured porous reactors are made of stainless steel with an internal diameter of 3.4 mm and were designed using the CAD software Solid Edge V20. The base structure of such a porous reactor is shown in Fig. 2. It consists of cylindrical fibres with an outer diameter of 250 μm in a stacking arrangement. In this study, we investigate two stacking arrangements, 1–3 and 1–3–5.[39] In 1–3, cylinders in consecutive layers are shifted by half of the inter-fibre distance, while in 1–3–5, cylinders in consecutive layers are shifted by a third of the inter-fibre distance (Fig. 2). These stacking arrangements can readily be manufactured using 3DFD, whereas SLS allows further design variations. The structured reactors made using the SLS technique consist of these two stacking arrangements consecutively arranged over each other, and additional rotations between fibre layers are

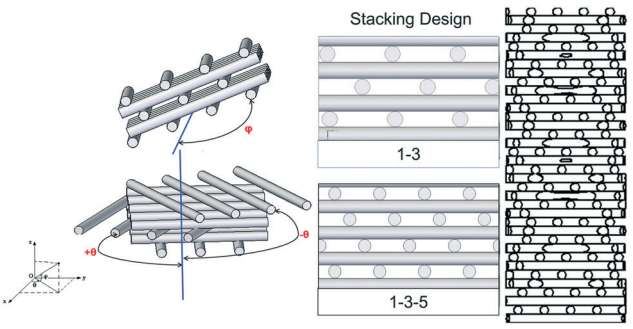

Fig. 2 Basic design of the porous structures, which consist of cylindrical fibres in a layered arrangement. The design parameters include the rotation of a fibre layer with respect to the *z*-axis (θ), the rotation with respect to the *x*,*y*-plane (φ), and the stacking arrangement (1–3 *vs.* 1–3–5).

introduced with respect to the mean flow direction (z-axis, angle θ) and with respect to the plane normal to the mean flow direction (x,y-plane, angle φ), see Fig. 2. Table 1 summarizes the geometric details of the structured porous reactors analyzed in the present study.

For benchmark purposes, the two-phase flow hydrodynamics and interfacial mass transfer in these novel porous structures are compared with conventional milli-scale packed bed reactors (entries PB 1 and PB 2 in Table 1) with an internal diameter of 3.8 mm. The first packed bed (PB 1) has an equivalent void volume to that of the porous reactors but a larger specific solid surface area due to the small size of the stainless steel spheres used as packing material. These packed bed characteristics correspond to reactors commonly encountered for bi-phasic reactions.[14] However, as the main source of pressure drop in the packed bed is the viscous dissipation on the introduced solid surfaces, an additional packed bed matching both void volume and specific surface area of the porous structures was prepared using larger glass spheres (PB 2). Consequently, both packed beds can be applied under identical operating conditions to those of the porous reactors, and their performance can therefore be used to benchmark the mass transfer performance and energy dissipation in the novel structures.

2.2. Experimental methods

The hydrodynamics and interfacial mass transfer in these porous flow reactors were characterized for two liquid–liquid systems, toluene–water and *n*-butanol–water (see Table 2 for their physical properties). For toluene–water, laser based optical measurements are established, while for *n*-butanol–water a chemical method is used to quantify interfacial mass transfer. All chemicals are of analytical grade and were used as received (Sigma Aldrich).

2.2.1. Optical measurements. We used 2D particle image velocimetry (PIV[43,44]) and planar laser induced fluorescence (PLIF[45]) to investigate the two-phase flow of water and toluene. Both phases are initially saturated with each other to ensure that only the mass transfer of a fluorescent dye from the water phase to the toluene phase is evaluated. Both phases are brought in contact through a Tee connection (internal diameter 1.25 mm), followed by a 2 cm PTFE tube coupled to a metal adapter (length 3 cm) with an internal diameter of 3.18 mm, which is then introduced into the reactor (internal diameter 3.4 mm). The flow rate ratio of both phases is 1 : 1, and the experiments are carried out at total volumetric flow rates of 1 ml min^{-1} and 3 ml min^{-1}, which are controlled using syringe pumps (CHEMYX Fusion 200). As the manufactured reactors are opaque, the outlet of the porous section is connected to a glass tube with identical internal diameter (3.4 mm) *via* a push-in connector. The flow at the end of this connection, approximately 2 cm downstream of the reactor outlet, is recorded using a dual Nd:YAG laser (LaVision, 65 mJ, 532 nm) and a high speed camera (LaVision Imager LX 2M) attached to a Zeiss Discovery.V20 stereomicroscope equipped with a Plan-Apochromat 1.0× objective. The resulting pixel resolution of the images is 1608 × 1208 pixels with an individual pixel size of 7.4 μm. The camera is fitted with a band pass filter (580 ± 10 nm) to block all wavelengths except for the emission of the fluorescent dye (PLIF) or particles (PIV). The temporal resolution for the PIV measurements is 3 Hz, while for the PLIF analysis a recording frequency of 1.5 Hz is used. In order to avoid image distortions due to the curved surface of the cylindrical glass tube, it is inserted in a rectangular visualization box filled with glycerol achieving an identical refractive index (index matching). The laser sheet (thickness 100 μm) enters the visualization box and glass tube from the side, while images are captured from the top as shown in Fig. 3.

PIV is applied to measure the velocity fields in the aqueous slugs, and therefore, the water phase is seeded with fluorescent particles (mean diameter of 10 μm) coated with Nile Red. The post processing of the PIV data is carried out using the commercial software Davis 8.2.2. For the cross-correlation to obtain the velocity fields, a multi-pass algorithm with interrogation areas of 128 × 128 pixels and 64 × 64 pixels is used, where a 50% overlap is applied on the final pass. A total of 2000 image pairs for 1 ml min^{-1} and 1000 image pairs

Table 2 Physical properties of the fluids used in this study[42]

	Fluid		
Properties	Water	Toluene	*n*-Butanol
Density, ρ (kg m^{-3})	998	867	810
Viscosity, η (Pa s)	1.00×10^{-3}	0.59×10^{-3}	2.95×10^{-3}
Interfacial tension, σ (N m^{-1})		3.30×10^{-2}	8.00×10^{-4}

Table 1 Geometric details of the manufactured porous structures

Name	Method	Void volume (μL)	Porosity (%)	Specific surface area (m^2 m^{-3})	Description
Vito	3DFD	437.9	72%	4480	1–3–5 design, $\varphi = 0°$ and $\theta = 0°$
Insp 1	SLS	449.6	74%	4160	$\theta = \pm 22.5°$ in alternate stacks, $\varphi = 45°$ around the x,y-plane
Insp 2	SLS	448.6	74%	4160	$\theta = \pm 45°$ in alternate stacks, $\varphi = 45°$ around the x,y-plane
Insp 3	SLS	450	74%	4160	$\theta = 0°$, 45°, 90°… for alternate rows, $\varphi = 45°$ around the x,y-plane
Insp 4	SLS	447.4	74%	4160	$\theta = 0°$ and $\varphi = 45°$ around the x,y-plane
Insp 5	SLS	449.6	70%	4800	$\theta = \pm 22.5°$ for alternate stacks and $\varphi = 0°$
PB 1	Packed bed	394.6	40%	37 895	Stainless steel spheres, particle size: 60–125 μm
PB 2	Packed bed	409.8	42%	4640	Glass spheres, particle size: 750 μm

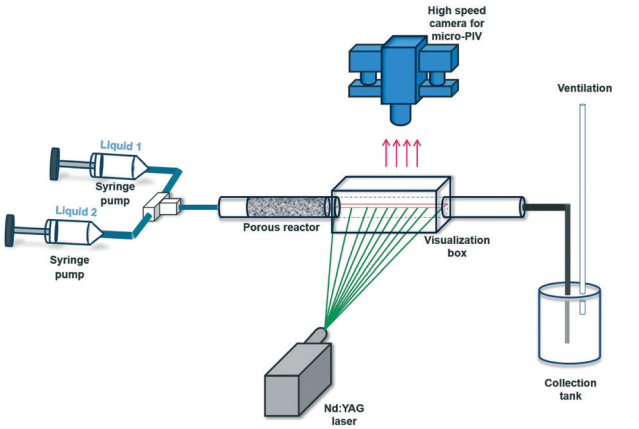

Fig. 3 Schematic representation of the experimental setup for optical measurements.

for 3 ml min^{-1} are captured at a frame rate of 3 Hz. In order to eliminate instantaneous spurious vectors, the average velocity field of each aqueous slug is calculated by a sliding average method using an in-house MATLAB code.

These PIV measurements are combined with PLIF to quantify the interfacial mass transfer of the fluorescent dye Rhodamine B (RhB). RhB is soluble in both water and toluene, but it only displays fluorescence in the water phase, whereas in the toluene phase it forms a colorless lactone.[46] For all experiments, the inlet concentration of the aqueous RhB solution ($C_{aq,i}$) is maintained at 22 μmol l^{-1}. A total of 1000 images for 1 ml min^{-1} and 600 images for 3 ml min^{-1} are captured at a frame rate of 1.5 Hz. The image post processing for PLIF is also carried out using the commercial software Davis 8.2.2. Further quantification of slug characteristics, *e.g.* slug length and void fraction, is carried out using an in-house MATLAB code.[47] The two phase PIV and PLIF results of the different structured porous reactors are further compared with an empty glass tube (ET) with identical internal diameter.

2.2.2. Chemical system. The effect of design parameters on the mass transfer in liquid–liquid flows is further quantified by a standard chemical test system using *n*-butanol and water with succinic acid as transfer species.[42] On the milliscale, this fluid combination establishes stratified flow due to the low interfacial tension.[15] Before each experiment, both phases are mutually saturated with each other, and 1 wt% succinic acid is added to *n*-butanol. A schematic of the experimental setup is shown in Fig. 4. Residence times between 5–50 s are achieved using syringe pumps (CHEMYX Fusion 200), and the two phases coming from the outlet of the reactor are instantaneously separated using an in-house built membrane based phase separator.[48] The aqueous phase is analyzed by titration with 0.1 N NaOH using phenolphthalein as a pH indicator.

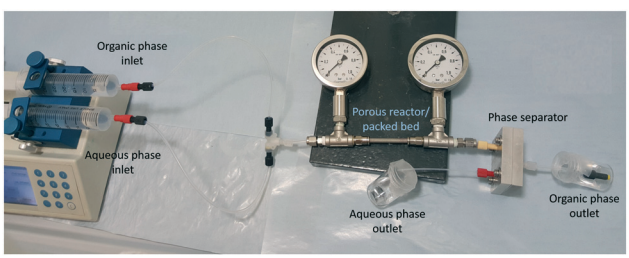

Fig. 4 Photograph of the experimental setup for chemical mass transfer measurements.

2.2.3. Estimation of the overall mass transfer coefficient. When the solubility of a solute, which is being transferred from one phase to a second phase, is sufficiently low to assume constant properties of the second phase, and if the mass transfer resistance lies entirely in the second phase (by mutually saturating both phases), the logarithmic mean driving force can be applied to determine the overall volumetric mass-transfer coefficient, k_La, according to[49]

$$k_L a = \frac{1}{\tau}\ln\left(\frac{C^*_{aq} - C_{aq,i}}{C^*_{aq} - C_{aq,o}}\right) \quad (1)$$

where k_L is the overall mass transfer coefficient, a is the specific interfacial area, $C_{aq,i}$ is the concentration of the transfer component in the water phase at the inlet and $C_{aq,o}$ is its concentration at the aqueous outlet. C^*_{aq} denotes the equilibrium concentration of the transfer component in the aqueous phase which is defined by the partition coefficient between the two phases.[42] The residence time τ is calculated from the reactor volume V_R and the volumetric flow rates Q_{aq} and Q_{org} according to

$$\tau = \frac{V_R}{Q_{aq} + Q_{org}} \quad (2)$$

The overall extraction can be quantified by calculating the extraction efficiency E, which describes the concentration difference reached between the channel inlet and outlet compared to the maximum possible concentration difference between the inlet concentration and the equilibrium concentration between the two phases

$$E(\%) = 100\cdot\left(\frac{C_{aq,i} - C_{aq,o}}{C_{aq,i} - C^*_{aq}}\right) \quad (3)$$

2.2.4. Pressure drop and energy dissipation. The pressure drop Δp over the porous reactors is measured by two pressure gauges (Capsule pressure gauge, Baumer, France) connected to the inlet and outlet of the reactor. This measurement allows for the calculation of the energy dissipation ε in the different reactors, according to[50]

$$\varepsilon = \frac{\Delta p\left(Q_{aq} + Q_{org}\right)}{\rho V_R} \quad (4)$$

where ρ denotes the phase-averaged density.

The pressure drop for the empty tube ET could not be accurately measured experimentally and was therefore calculated using the homogeneous two-phase flow model.[51,52]

3. Results

3.1. Hydrodynamic study

The combination of PIV and PLIF allows a detailed hydrodynamic study of the two-phase distribution of the toluene–water system downstream of the different porous reactors. For the chosen operating conditions, the two-phase flow of toluene–water is established as slug flow in an empty tube as the interfacial tension is sufficiently large to stabilize individual slugs.[53]

The averaged slug length of the continuous water phase and dispersed toluene phase is measured using PLIF and is plotted in Fig. 5 for a total flow rate of 1 ml min^{-1}. As we observe an alternating sequence of uniform water and toluene slugs in the empty tube, these values are used for normalization of the slug length obtained in the porous reactors, as this allows a clear visualization of the effect of the porous structures. For the reactors Vito, Insp 1, and Insp 3, a combination of long and short water slugs is observed (Fig. 5(a)), indicating the breakup of the continuous water phase through the interaction with the porous structure. For these structures, the dispersed toluene phase is also split into long, medium and short slugs (Fig. 5(b)). These 3 categories are defined based on the maximum slug length of each porous reactor, short slugs are smaller than 20% of the maximum, long slugs are larger than 80% of the maximum, and medium slugs are in between these values. The other porous structures (Insp 2, Insp 4, and Insp 5) exhibit an alternating sequence of uniform water and toluene slugs at this flow rate. However, it is also worth noting that all porous structures result in shorter slug sizes compared to the empty tube case, which is especially pronounced for the Insp 2 reactor

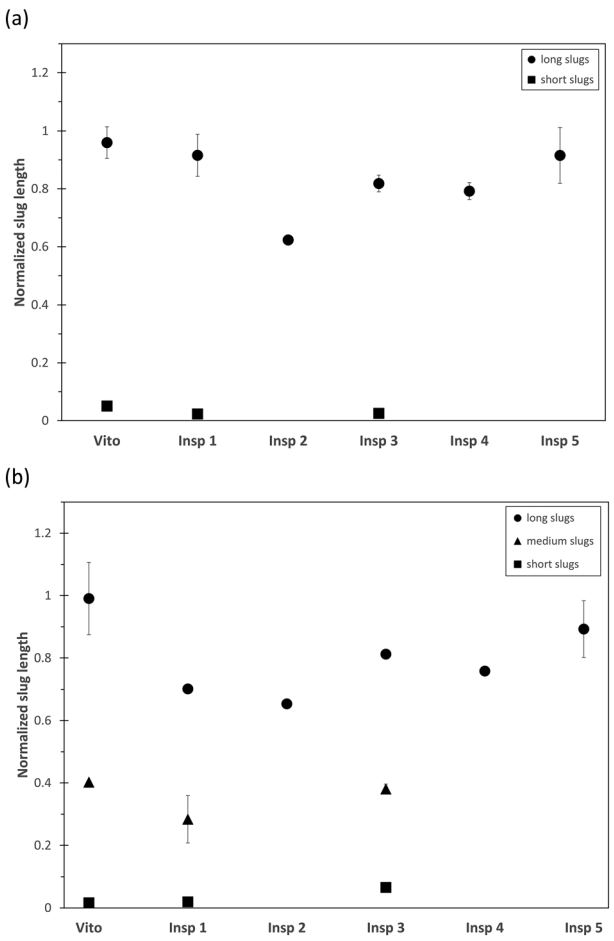

Fig. 5 Normalized averaged slug lengths of the continuous water phase (a) and dispersed toluene phase (b) for a total flow rate of 1 ml min^{-1}. The bars indicate the standard deviation in the measured slug lengths.

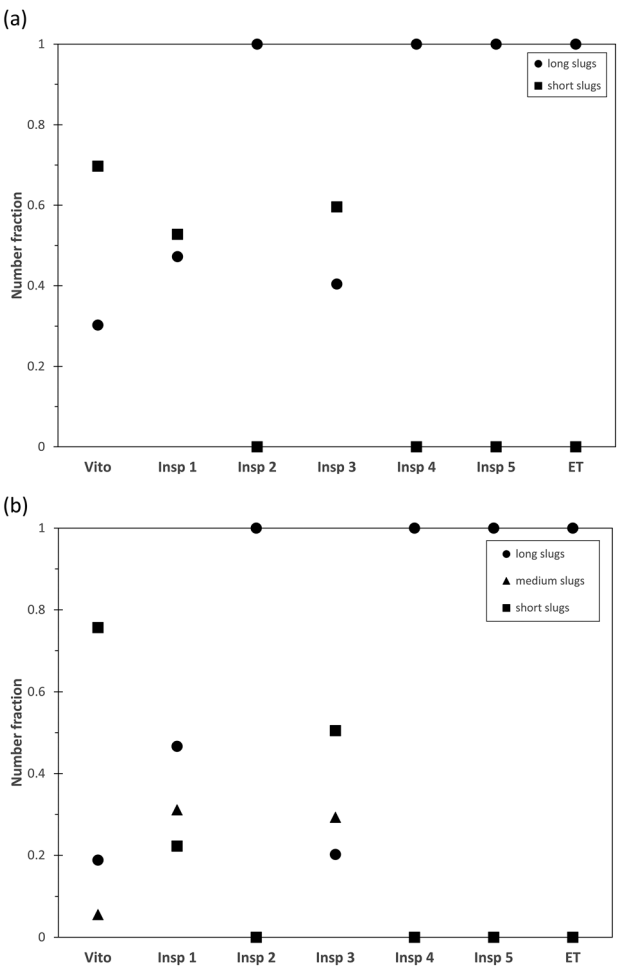

Fig. 6 Distribution of slug sizes of the continuous water phase (a) and dispersed toluene phase (b) for a total flow rate of 1 ml min^{-1}.

which shows a slug size reduction of around 40%. Furthermore, it needs to be highlighted that we determined the slug sizes 2 cm downstream of the structure, as such obtained results are indicative of the hydrodynamics inside the structures but are not able to yield local information on *e.g.* the two-phase slip inside the porous structure.

Fig. 6 depicts the number distribution of the different slug sizes of the continuous water phase and dispersed toluene phase for a total flow rate of 1 ml min^{-1}. An equal number fraction of short and long slugs indicates an alternating pattern, while a larger number fraction of short slugs indicates that more than one short slug is in between two long slugs. In the case of the water phase (Fig. 6(a)), it is observed that the 3 structures leading to slug breakup (Vito, Insp 1, and Insp 3) generate a larger number of short slugs. This is also true for the toluene phase (Fig. 6(b)) for the Vito and Insp 3 structure, resulting in the least amount of medium and long slugs for these two structures. This increased slug breakup of the toluene phase is not observed for the Insp 1 structure. When increasing the total flow rate to 3 ml min^{-1}, all porous reactors induce slug breakup due to the increased shear forces acting inside the structure (Fig. 7). Similar to the total flow rate of 1 ml min^{-1}, the resulting mean slug lengths of the water and toluene phases are smaller compared to the empty tube due to slug breakup. This is also true for the Insp 1 structure, where the long slugs of the water and toluene phases are 20% and 5% larger than in the empty tube case (indicating coalescence at the outlet of the porous reactor before the measurement location) but where also more medium and short size slugs are generated in each phase (Fig. 8). Comparing the obtained slug sizes and their respective number fraction between flow rates (Fig. 5–8), it is observed that an increase in flow rate leads to a decrease in the slug length, and this effect is more pronounced for the dispersed toluene slugs. For structures Insp 1 to Insp 5, an increase in flow rate leads to an increase in the number of short and medium sized slugs in both phases (Fig. 6 and 8), which indicates an increased slug breakup for these porous reactors with increasing shear forces.

Interestingly, this behavior is not observed in the Vito structure, where the number fraction of short water slugs decreases with increasing flow rate. Furthermore, in the toluene phase, the number fraction of medium slugs increases with

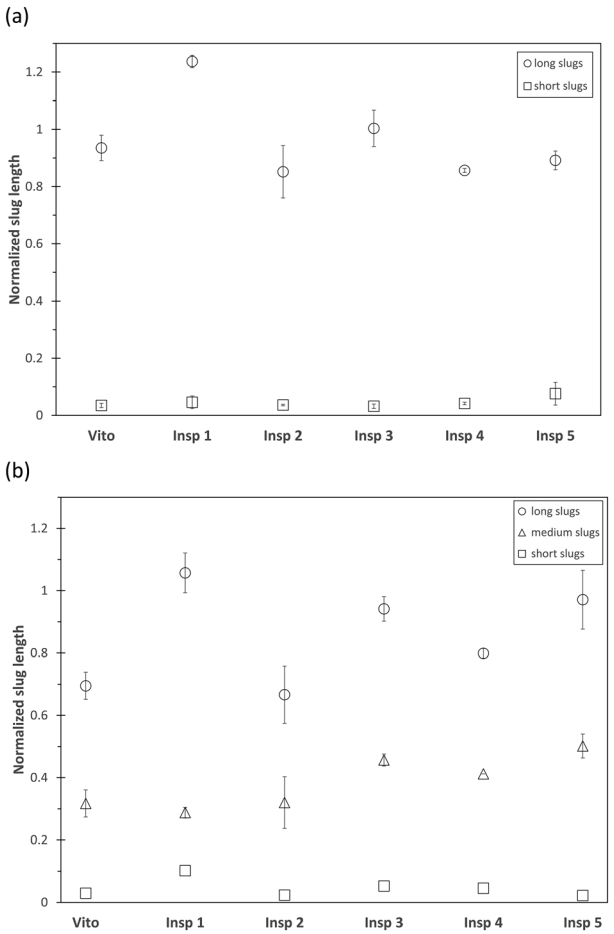

Fig. 7 Normalized averaged slug lengths of the continuous water phase (a) and dispersed toluene phase (b) for a total flow rate of 3 ml min^{-1}. The bars indicate the standard deviation in the measured slug lengths.

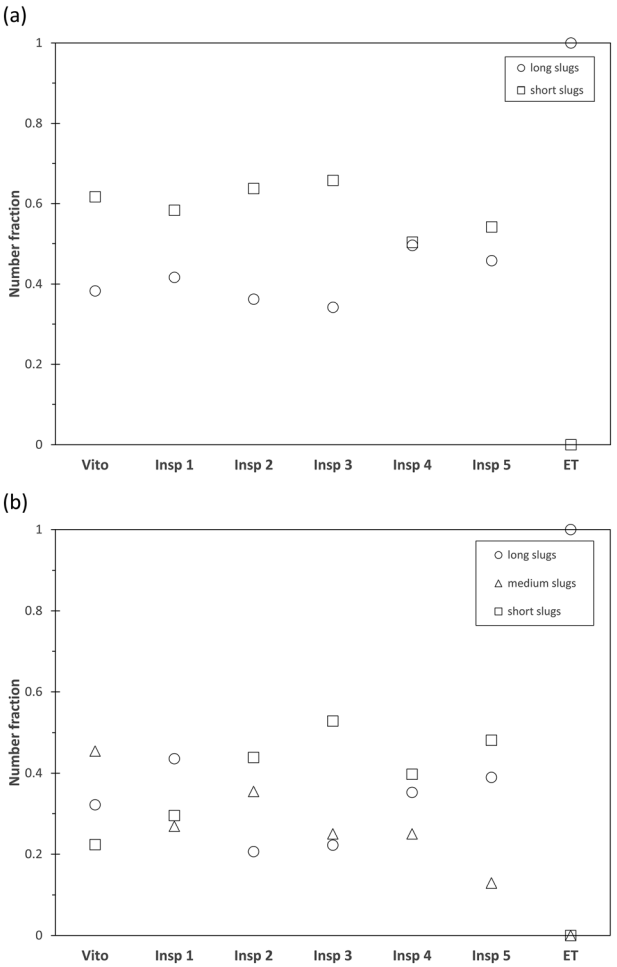

Fig. 8 Distribution of slug sizes of the continuous water phase (a) and dispersed toluene phase (b) for a total flow rate of 3 ml min^{-1}.

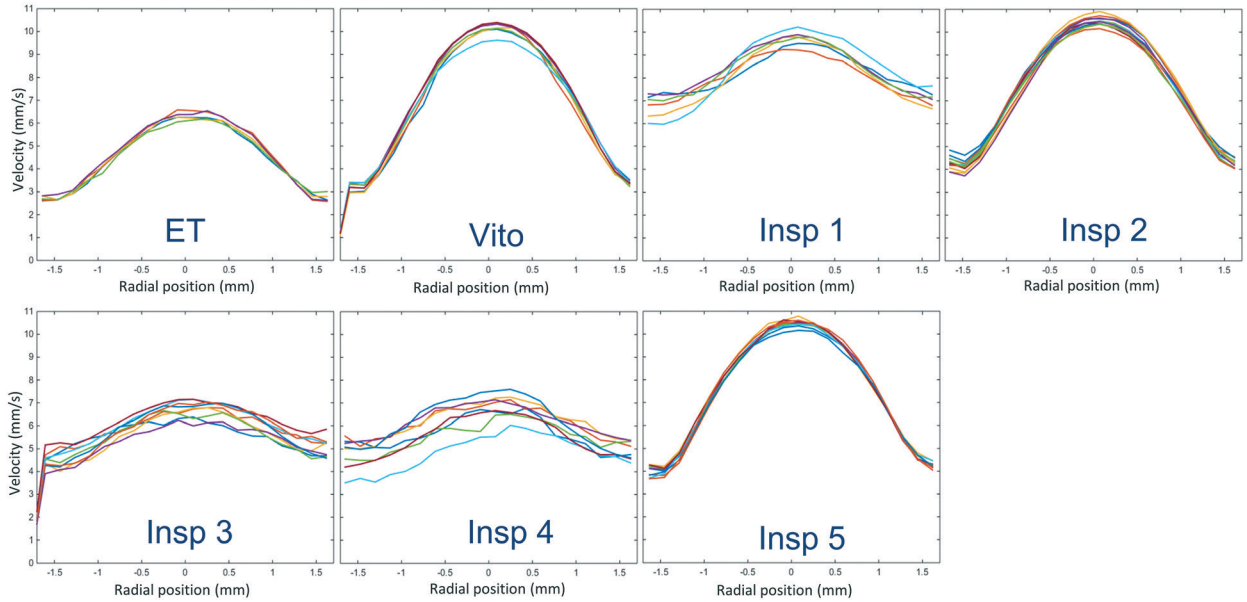

Fig. 9 Profiles of the local phase velocity averaged over the length of the water slug for a total flow rate of 3 ml min^{-1}. Each solid line represents the streamwise averaged velocity profile of an individual water slug.

an increase in flow rate, while the number fraction of short slugs is decreasing as well. This indicates a reduction in slug breakup efficiency when increasing the shear forces inside this particular porous structure. The major geometrical difference between the Vito and the Insp porous reactors is the lack of rotation between the fibre layers in the Vito design, thus the reduced slug breakup could be explained by channeling effects enabled by its design.

In addition to the distribution of slug sizes in each phase, we also investigated the individual slug velocities. 2D PIV is used to measure the local velocity distribution in each water slug, and the mean local phase velocity averaged over the length of the water slug is depicted in Fig. 9 for a total flow rate of 3 ml min^{-1}. In this figure, each solid line represents the streamwise averaged velocity profile of an individual water slug. The obtained velocity profiles for 1 ml min^{-1} are identical and will not be presented here for brevity. The velocity profiles of the water phase in the empty tube correspond to fully developed slug flow, and hence any deviation from these profiles indicates the influence of the porous structure. It is observed that the porous reactors Insp 3 and Insp 4 exhibit velocity profiles similar to the empty tube, suggesting that the effects of these particular porous structures on the phase velocity are negligible as the profiles redevelop to their original shape rather quickly. The porous reactors Vito, Insp 2, and Insp 5 show a steep parabolic velocity profile. For the Insp 2 structure, this can be explained by the fact that this structure generates smaller slugs for both the water phase and the toluene phase, which then results in these steep parabolic velocity profiles. On the other hand, for the Vito and Insp 5 structures, we observe long slugs, which is another indication of the aforementioned channeling in these structures, also resulting in steep velocity profiles. The porous reactor Insp 1 exhibits the largest deviation from the

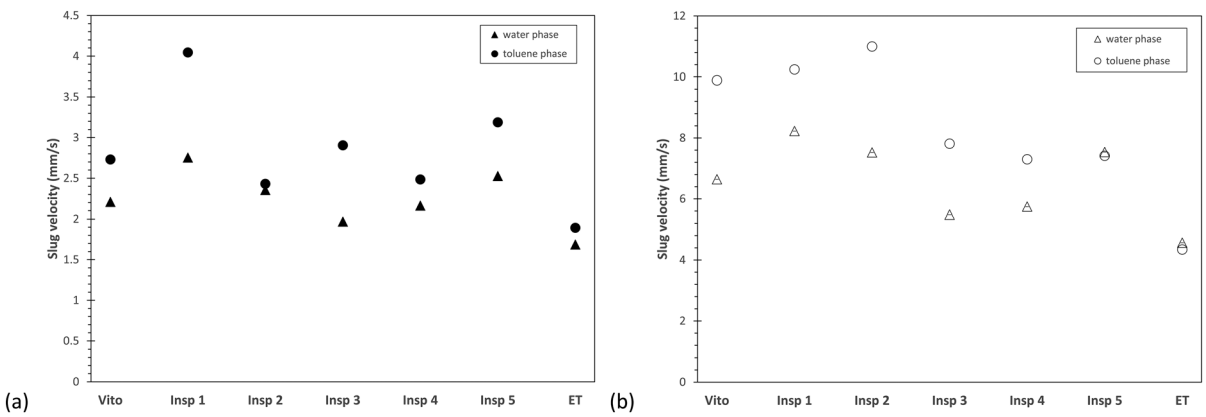

Fig. 10 Average slug velocities of the continuous water phase and dispersed toluene phase for total flow rates of (a) 1 ml min^{-1} and (b) 3 ml min^{-1}.

developed empty tube velocity profile, also in its relatively flat profile, but more pronounced by the fact that the maximum velocity is two times larger compared to the empty tube. This indicates that the effect of this particular porous structure on the original slug flow is largest, as it is still redeveloping into its original pattern at the measurement location.

In Fig. 10, the averaged phase velocities of the water and toluene phases for both flow rates of 1 ml min^{-1} and 3 ml min^{-1} are compared. The averaged phase velocity of the water phase is obtained by averaging the PIV profiles shown in Fig. 9, and the phase velocity of the toluene phase is calculated from the PLIF measurements which allows the determination of the two-phase slip. Compared to the developed slug flow in the empty tube, all porous reactors lead to an increased velocity for both phases, which is expected as the presence of the porous structures reduces the available flow cross-section and thus results in higher local phase velocities. At both flow rates, the porous reactor Insp 1 exhibits the largest velocities of the water and toluene phases, which further illustrate the large influence of this particular porous design on slug flow. Furthermore, the toluene phase velocity is always greater compared to the water phase velocity. As toluene is the dispersed phase (also in the stainless steel porous structure), it will occupy a smaller cross-section, which then results in the observed velocity difference. This velocity difference, in combination with the overall phase velocity, will also lead to the development of secondary flow structures, which will affect interfacial mass transfer.

3.2. Mass transfer characterization

For the toluene–water system, the overall volumetric mass transfer coefficient k_La is obtained using the PLIF technique with RhB as transfer species. The toluene–water–RhB system is characterized by a large distribution coefficient of 760,[46] which means that the transfer of RhB from the interface to the toluene phase is favored, while the transfer of RhB from the bulk of the water phase to the interface is the rate limiting step. Therefore, this system allows one to characterize the influence of the individual phase velocities and slug sizes on the overall mass transfer performance. The overall volumetric mass transfer coefficient k_La for the different porous reactors in comparison to the empty tube is depicted in Fig. 11.

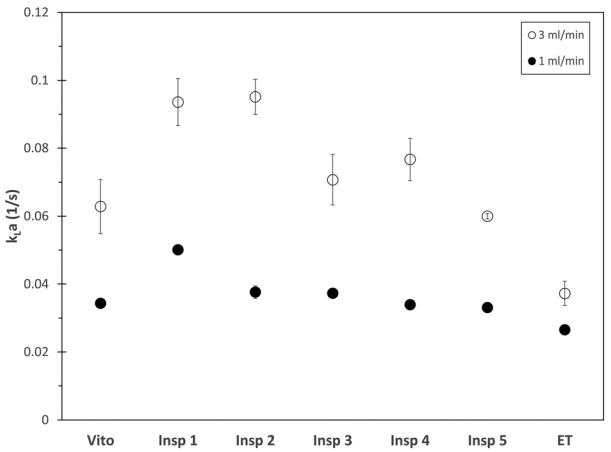

Fig. 11 Overall mass transfer coefficient k_La for the different porous reactors and the empty tube for total flow rates of 1 ml min^{-1} (closed symbols) and 3 ml min^{-1} (open symbols), with bars indicating the standard deviation.

For both considered flow rates, the porous reactors result in an increased mass transfer coefficient compared to the empty tube. Furthermore, for all considered reactors, the overall mass transfer coefficient increases with increasing flow rate. Moreover, for the lower flow rate, the porous reactor Insp 1 results in the largest k_La value, whereas for the higher flow rate the reactors Insp 1 and Insp 2 exhibit the best mass transfer performance. As outlined above, the resistance to mass transfer is located in the bulk water phase, and consequently, the surface renewal velocities inside the water slug as well as the number fraction of short water slugs will directly influence the observed mass transfer. As such, the mass transfer performance of the individual porous reactors is supported by the hydrodynamic study. For a total flow rate of 1 ml min^{-1}, the Insp 1 structure is characterized by the largest velocities of the water and toluene phases, together with a large phase velocity difference and a high number fraction of short water slugs. Increasing the total flow rate to 3 ml min^{-1}, the Insp 2 structure will become equally effective as it also shows increased phase velocities and a large number fraction of short slugs. On the other hand, the porous reactor Insp 5 also showed increased water phase velocity, however paired with a limited phase velocity difference and a low number fraction of short slugs, and thus a lower overall mass transfer is observed. The combination of long water slugs with increased phase velocity observed for this structure can also be attributed to the aforementioned channeling phenomena. For the porous reactors Vito and Insp 3, a large number fraction of short slugs is observed, but their phase velocity is low, resulting in a comparatively lower mass transfer performance. The Insp 4 structure results in the lowest number fraction of short slugs, together with low phase velocities, and consequently also comparatively low k_La values are observed.

As mentioned above, the undisturbed water–toluene system in an empty tube will be established as elongated slug flow, and it has been shown that asymmetrical recirculation patterns within individual slugs enhance mass transfer.[54] Such asymmetrical recirculation patterns can be generated when meandering channels are used.[55] The analogy to meandering channels can be used to explain the increased mass transfer performance of the Insp 1 and Insp 2 structures compared to the other porous reactors. In these two structures, all design parameters are varied simultaneously, whereas all other structures only alter one or two parameters at a time. This increased degree of freedom in the design of Insp 1 and Insp 2 leads to a non-uniform channel path, which in turn results in improved inter-phase penetration and mass transfer coefficients.

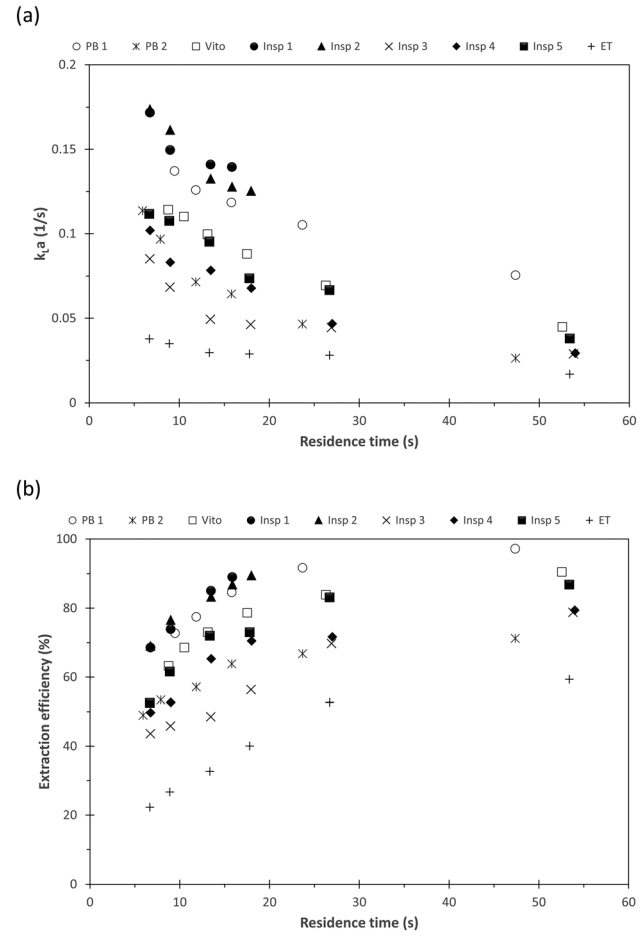

Fig. 12 (a) Overall mass transfer coefficient k_La and (b) extraction efficiency for the different porous reactors and packed beds using the *n*-butanol–water–succinic acid system.

We then extended the mass transfer study using the *n*-butanol–water system with succinic acid as transfer species. While toluene–water is characterized by a large interfacial tension and slug flow, *n*-butanol–water has a low interfacial tension which then results in stratified flow.[15] As a benchmark, the mass transfer performance of the porous reactors is compared with those of the two packed beds of comparable void volume but varying specific solid surface areas (Table 1). The observed overall volumetric mass transfer coefficient k_La is depicted in Fig. 12(a). For all considered reactors, the usual trend of increasing mass transfer with decreasing residence time is found. The results also demonstrate that the porous reactors Insp 1 and Insp 2 exhibit the largest mass transfer coefficients, approximately 14% larger than the observed values for the packed bed reactor PB 1 with similar void volume but significantly larger specific solid surface area. This is further illustrated by the extraction efficiency, depicted in Fig. 12(b). Complete mass transfer is obtained for these two porous reactors for residence times exceeding 20 s as the extraction efficiency reaches 100%, which further highlights their mass transfer improvements for low interfacial tension fluid pairs. Furthermore, and similar to the toluene–water system, in comparison with the Insp 1 structure, Insp 2 exhibited improved mass transfer performance with increasing flow rate (decreasing residence time). The observed k_La value of Insp 2 is smaller than Insp 1 for residence times above 10 s, but below this residence time a larger k_La is observed, which further illustrates that this particular design is beneficial for higher flow rates. All other porous reactors have a lower mass transfer coefficient compared to Insp 1, Insp 2, and PB 1. It is worth highlighting that the packed bed PB 2 with similar void volume and specific solid surface area to those of the porous structures exhibits comparatively low mass transfer coefficients which are found to be smaller than Insp 4 and Insp 5, only exceeding Insp 3 and the empty tube ET. This highlights the improved performance of the designed porous structures, which on average increases mass transfer compared to packed beds with similar void volume and similar specific solid surface area.

As the *n*-butanol–water system is established as stratified flow, the enhancement of interfacial mass transfer is directly correlated with the degree of radial mixing, whereas for the toluene–water system established as slug flow improved inter-phase penetration is more important. Comparing the obtained mass transfer coefficients, we can conclude that the porous reactors Insp 1 and Insp 2 enhance both inter-phase penetration and radial mixing, since the largest k_La values are observed for both fluid pairs. As outlined above, this can be explained by the non-uniform channel path, which is achieved by simultaneously varying all design parameters throughout the porous structure. Insp 3 and Insp 4 perform better for toluene–water but worse for *n*-butanol–water compared to the Vito and Insp 5 structures. Consequently, the Insp 3 and Insp 4 structures achieve comparatively larger inter-phase penetration, which can be related to their geometry as they introduce a rotation with respect to the plane normal to the mean flow direction (x,y-plane, angle φ). On the contrary, the Vito and Insp 5 structures are characterized by a radial offset and a rotation of fibre layers with respect to the mean flow direction (z-axis, angle θ), respectively. This

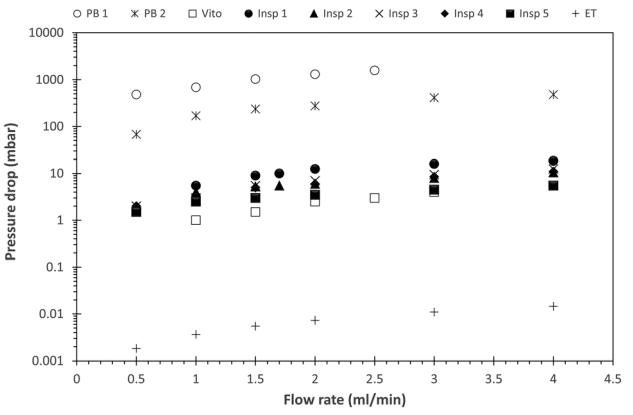

Fig. 13 Pressure drop across the porous reactors for varying total flow rates. The pressure drop is plotted on a logarithmic scale to accommodate the visibility of the data points in a single figure.

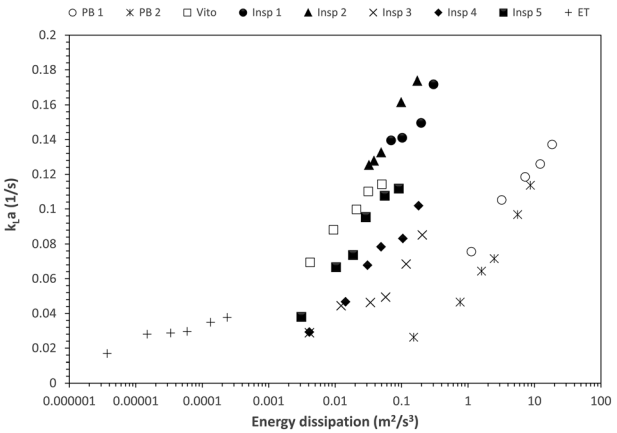

Fig. 14 Overall mass transfer coefficient k_La as a function of the energy dissipation ε in the porous reactors. Energy dissipation is plotted on a logarithmic scale to accommodate the visibility of the data points in a single figure.

leads to an increase in radial mixing and consequently a comparatively better mass transfer performance for the *n*-butanol–water system.

3.3. Pressure drop and energy dissipation

In order to quantify the mass transfer performance of each reactor, it is important to consider the energy required to achieve the observed k_La values. This energy input is related to the pressure drop across the porous reactor, which is depicted in Fig. 13 for the *n*-butanol–water system at different total flow rates. For the studied range of operating conditions, a linear relationship between pressure drop and flow rate is observed, which indicates that turbulence inside the porous structures is negligible. Furthermore, it is evident that all porous reactors are characterized by a significantly lower pressure drop compared to the packed bed reactors, where PB 1 exhibits the largest pressure drop due to viscous dissipation at the comparatively large solid surface area. However, the pressure drop induced by PB 2 with similar specific solid surface area as the designed porous structures is still an order of magnitude larger compared to them. Within the structured porous reactors, and at a given flow rate, Vito and Insp 5 yield the lowest pressure drop values, which might again signify channeling effects in these two designs. The reactors Insp 2, Insp 3 and Insp 4 experience similar pressure drop across all flow rates, and the largest pressure drop is experienced by the reactor Insp 1.

However, when considering the energy dissipation, the reactor Insp 1 has the best overall performance across all flow rates (Fig. 14). The porous structure Insp 2 only achieves larger mass transfer coefficients at elevated energy dissipation (increased flow rates). Comparing the different porous reactors, the second best mass transfer performance is achieved by Vito and Insp 5, which is connected to their improvement in radial mixing, while Insp 3 and Insp 4 perform least good. However, it has to be noted that for comparable k_La values, all structured porous reactors result in an order of magnitude lower energy dissipation compared to the packed bed reactors. This clearly highlights the potential of structured porous reactors for their application in efficient chemical processes.

4. Conclusions

A hydrodynamic study of novel designed porous milli-scale reactors for improved mass transfer in an immiscible liquid–liquid flow system is carried out using PIV and PLIF. The obtained results are compared with an empty tube case, and the results illustrate that porous reactors induce slug breakup and thus inter-phase penetration especially at higher flow rates. Consequently, the resulting mean slug lengths of the individual phases are significantly reduced compared to the empty tube. The geometry of the porous reactors greatly affects the velocity profile in the slugs, and porous designs with no structural variation in the streamwise direction (Vito and Insp 5) are susceptible to channeling. However, all porous reactors result in enhanced local phase velocities.

The effect of these different hydrodynamics is further observed when quantifying the interfacial mass transfer. For this, we considered the slug flow (in an empty tube) of toluene–water (RhB as transfer species) and the stratified flow (in an empty tube) of *n*-butanol–water (succinic acid as transfer species). By addressing different flow regimes, we have identified the link between the orientation of the constituting layers of the porous geometry and if it is able to enhance inter-phase penetration and/or radial mixing. Overall, the porous reactors Insp 1 and Insp 2 have been identified as the most promising designs, as they result in the largest k_La values for both flow regimes. These particular designs are characterized by a non-uniform channel path, which is achieved by simultaneously varying all design parameters throughout the porous structure, most importantly rotations parallel and normal to the mean flow directions. Having only a single component of rotation results in lower mass transfer performance for either slug or stratified flow.

This study also highlights that structured porous reactors achieve the same order of interfacial mass transfer performance as packed bed reactors but at orders of magnitude lower energy dissipation. This clearly proves their potential for integration in novel flow reactors.

Nomenclature

Roman symbols

a	Interfacial area ($m^2\ m^{-3}$)
C	Concentration (mol l^{-1})
E	Extraction efficiency
k_La	Overall mass transfer coefficient (1/s)
Δp	Pressure drop (Pa)
Q	Flow rate (ml min^{-1})
V_R	Reactor volume (m^3)
x, y, z	Cartesian coordinates

Greek symbols

ε Energy dissipation ($m^2\ s^{-3}$)
η Viscosity (Pa s)
φ Rotation angle with respect to the x,y-plane
θ Rotation angle around the z-axis
ρ Density ($kg\ m^{-3}$)
σ Interfacial tension ($N\ m^{-1}$)
τ Residence time (s)

Abbreviations

3DFD 3 Dimensional fibre deposition
PIV Particle image velocimetry
PLIF Planar laser induced fluorescence
RhB Rhodamine B
SLS Selective laser sintering

Acknowledgements

We thank Adriaan Spierings (inspire AG – innovation center for additive manufacturing, Switzerland) for manufacturing the custom designed porous reactors. S. K. acknowledges funding from Marie Curie CIG and FWO-Odysseus II.

References

1 R. L. Hartman, J. P. McMullen and K. F. Jensen, *Angew. Chem., Int. Ed.*, 2011, **50**, 7502–7519.
2 K. F. Jensen, B. J. Reizman and S. G. Newman, *Lab Chip*, 2014, **14**, 3206–3212.
3 J. P. McMullen and K. F. Jensen, *Annu. Rev. Anal. Chem.*, 2010, **3**, 19–42.
4 T. Razzaq and C. O. Kappe, *Chem. – Asian J.*, 2010, **5**, 1274–1289.
5 V. Hessel and T. Noël, in *Ullmann's Encyclopedia of Industrial Chemistry*, Wiley-VCH Verlag GmbH & Co. KGaA, 2012, DOI: 10.1002/14356007.q16_q01.
6 V. Hessel and T. Noël, in *Ullmann's Encyclopedia of Industrial Chemistry*, Wiley-VCH Verlag GmbH & Co. KGaA, 2012, DOI: 10.1002/14356007.b16_b37.pub2.
7 A. Adamo, R. L. Beingessner, M. Behnam, J. Chen, T. F. Jamison, K. F. Jensen, J.-C. M. Monbaliu, A. S. Myerson, E. M. Revalor, D. R. Snead, T. Stelzer, N. Weeranoppanant, S. Y. Wong and P. Zhang, *Science*, 2016, **352**, 61–67.
8 B. Gutmann, D. Cantillo and C. O. Kappe, *Angew. Chem., Int. Ed.*, 2015, **54**, 6688–6728.
9 S. Mascia, P. L. Heider, H. Zhang, R. Lakerveld, B. Benyahia, P. I. Barton, R. D. Braatz, C. L. Cooney, J. M. B. Evans, T. F. Jamison, K. F. Jensen, A. S. Myerson and B. L. Trout, *Angew. Chem., Int. Ed.*, 2013, **52**, 12359–12363.
10 P. Poechlauer, J. Manley, R. Broxterman, B. Gregertsen and M. Ridemark, *Org. Process Res. Dev.*, 2012, **16**, 1586–1590.
11 M. N. Kashid, A. Renken and L. Kiwi-Minsker, *Chem. Eng. Sci.*, 2011, **66**, 3876–3897.
12 V. Hessel, P. Angeli, A. Gavriilidis and H. Löwe, *Ind. Eng. Chem. Res.*, 2005, **44**, 9750–9769.
13 M. W. Losey, M. A. Schmidt and K. F. Jensen, *Ind. Eng. Chem. Res.*, 2001, **40**, 2555–2562.
14 J. R. Naber and S. L. Buchwald, *Angew, Chem., Int. Ed.*, 2010, **49**, 9469–9474.
15 A. Woitalka, S. Kuhn and K. F. Jensen, *Chem. Eng. Sci.*, 2014, **116**, 1–8.
16 J. Banhart, *Int. J. Vehicle Des.*, 2005, **37**, 114–125.
17 F. Baumgärtner, I. Duarte and J. Banhart, *Adv. Eng. Mater.*, 2000, **2**, 168–174.
18 A. Bhattacharya, V. V. Calmidi and R. L. Mahajan, *Int. J. Heat Mass Transfer*, 2002, **45**, 1017–1031.
19 K. Boomsma, D. Poulikakos and F. Zwick, *Mech. Mater.*, 2003, **35**, 1161–1176.
20 T. J. Lu, H. A. Stone and M. F. Ashby, *Acta Mater.*, 1998, **46**, 3619–3635.
21 M. S. Phanikumar and R. L. Mahajan, *Int. J. Heat Mass Transfer*, 2002, **45**, 3781–3793.
22 C. Hutter, A. Zenklusen, R. Lang and P. Rudolf von Rohr, *Chem. Eng. Sci.*, 2011, **66**, 1132–1141.
23 A. Montillet, J. Comiti and J. Legrand, *Chem. Eng. J.*, 1993, **52**, 63–71.
24 J. G. Fourie and J. P. Du Plessis, *Chem. Eng. Sci.*, 2002, **57**, 2781–2789.
25 D. Butscher, C. Hutter, S. Kuhn and P. Rudolf von Rohr, *Exp. Fluids*, 2012, **53**, 1123–1132.
26 C. Hutter, C. Allemann, S. Kuhn and P. Rudolf von Rohr, *Chem. Eng. Sci.*, 2010, **65**, 3169–3178.
27 C. Hutter, A. Zenklusen, S. Kuhn and P. Rudolf von Rohr, *Chem. Eng. Sci.*, 2011, **66**, 519–529.
28 M. V. Twigg and J. T. Richardson, *Ind. Eng. Chem. Res.*, 2007, **46**, 4166–4177.
29 M. D. Das, A. N. Hrymak and M. H. I. Baird, *Chem. Eng. Sci.*, 2013, **101**, 329–344.
30 F. Theron, N. Le Sauze and A. Ricard, *Ind. Eng. Chem. Res.*, 2010, **49**, 623–632.
31 C. P. Stemmet, J. N. Jongmans, J. van der Schaaf, B. F. M. Kuster and J. C. Schouten, *Chem. Eng. Sci.*, 2005, **60**, 6422–6429.
32 C. P. Stemmet, M. Meeuwse, J. van der Schaaf, B. F. M. Kuster and J. C. Schouten, *Chem. Eng. Sci.*, 2007, **62**, 5444–5450.
33 C. P. Stemmet, J. Van Der Schaaf, B. F. M. Kuster and J. C. Schouten, *Chem. Eng. Res. Des.*, 2006, **84**, 1134–1141.
34 M. Serres, M.-L. Zanota, R. Philippe and V. Vidal, *Int. J. Multiphase Flow*, 2016, **85**, 157–163.
35 J.-N. Tourvieille, R. Philippe and C. de Bellefon, *Chem. Eng. Sci.*, 2015, **126**, 406–426.
36 J.-N. Tourvieille, R. Philippe and C. de Bellefon, *Chem. Eng. J.*, 2015, **267**, 332–346.
37 L. Lü, J. Y. H. Fuh and Y. S. Wong, in *Laser-Induced Materials and Processes for Rapid Prototyping*, Springer US, Boston, MA, 2001, pp. 89–142, DOI: 10.1007/978-1-4615-1469-5_5.
38 A. B. Spierings, N. Herres and G. Levy, *Rapid Prototyp. J.*, 2011, **17**, 195–202.

39 J. Lefevere, M. Gysen, S. Mullens, V. Meynen and J. Van Noyen, *Catal. Today*, 2013, **216**, 18–23.
40 S. Danaci, L. Protasova, J. Lefevere, L. Bedel, R. Guilet and P. Marty, *Catal. Today*, 2016, **273**, 234–243.
41 J. Luyten, S. Mullens and I. Thijs, *KONA Powder Part. J.*, 2010, **28**, 131–142.
42 T. Misek, R. Berger and J. Schröter, *Standard test systems for liquid extraction*, Institute of Chemical Engineers, 1985.
43 D. C. Meinhart, T. S. Wereley and G. J. Santiago, *Exp. Fluids*, 1999, **27**, 414–419.
44 G. J. Santiago, T. S. Wereley, D. C. Meinhart, J. D. Beebe and J. R. Adrian, *Exp. Fluids*, 1998, **25**, 316–319.
45 J. P. Crimaldi, *Exp. Fluids*, 2008, **44**, 851–863.
46 H. Watarai and F. Funaki, *Langmuir*, 1996, **12**, 6717–6720.
47 S. Fransen and S. Kuhn, *React. Chem. Eng.*, 2016, **1**, 288–299.
48 M. E. Leblebici, S. Kuhn, G. D. Stefanidis and T. Van Gerven, *Chem. Eng. J.*, 2016, **293**, 273–280.
49 R. P. Verma and M. M. Sharma, *Chem. Eng. Sci.*, 1975, **30**, 279–292.
50 T. Vandermeersch, R. Goovaerts, J. Luyten, J. F. M. Denayer and W. De Malsche, *Chem. Eng. J.*, 2015, **279**, 9–17.
51 D. R. H. Beattie and P. B. Whalley, *Int. J. Multiphase Flow*, 1982, **8**, 83–87.
52 H. Müller-Steinhagen and K. Heck, *Chem. Eng. Process.: Process Intesif.*, 1986, **20**, 297–308.
53 H. S. Joshua, D. Tice, A. D. Lyon and R. F. Ismagilov, *Langmuir*, 2003, **19**, 9127–9133.
54 D. Fries, S. Waelchli and P. Rudolf von Rohr, *Chem. Eng. J.*, 2008, **135**, S37–S45.
55 P. Plouffe, D. M. Roberge, J. Sieber, M. Bittel and A. Macchi, *Chem. Eng. J.*, 2016, **285**, 605–615.

